Title

Invadopodia enable cooperative invasion and metastasis of breast cancer cells

Authors

L. Perrin,[1] B. Bayarmagnai,[1] E. Tuzël,[1,2] B. Gligorijevic[1,3]

Affiliations

[1]Bioengineering Department
Temple University
Philadelphia PA, USA.

[2]Department of Physics
Worcester Polytechnic Institute
Worcester MA, USA.

[3]Cancer Signaling & Epigenetics Program
Fox Chase Cancer Center
Philadelphia PA, USA.

Abstract

Multiple clones of cancer cells can seed metastases via collective invasion and dissemination. While it is known that cancer clones cooperate during invasion, the events leading to it and the effects it may have on metastasis are not known. In this study, we demonstrate that the 4T1 and 67NR breast cancer cell lines, which are clones isolated from the same metastatic tumor, sort from each other and go on to perform cooperative invasion. By time-lapse microscopy of heterogenous spheroids, we show that the invasive 4T1 cells migrate from the spheroid core to the spheroid edge and remain there, while the non-invasive 67NR cells move only within their initial compartment, resulting in cell sorting. Following cell sorting, 4T1 cells lead the 67NR cells in cooperative invasion strands. Knockdown of the invadopodia protein Tks5 in 4T1 cells demonstrates that invasion requires invadopodia only in leader cells, and not in follower cells. Importantly, in the lung clonogenic assay, we demonstrate that cells without invadopodia can engage in cooperative metastasis. Altogether, our results suggest that a few cells with invadopodia could be sufficient to drive the metastasis of cell clusters from heterogeneous tumors.

Introduction

More than 90% of cancer patients die due to complications resulting from metastasis, *i.e.* the process of dissemination, re-seeding and growth of cancer cells in secondary organs *(1, 2)*. In breast cancer, recent work demonstrated that metastases mostly arise from polyclonal seeding *(3, 4)*. These polyclonal metastases develop from the collective dissemination of cell clusters, as opposed to the successive accumulation of multiple single clones. Together with the growing literature on phenotypic heterogeneity within primary tumors *(5)*, these observations suggest that cooperativity between clones of cancer cells may facilitate metastasis.

In breast cancer, the metastatic cascade is initiated when cancer cells acquire invasive properties, which include motility and the ability to degrade the extracellular matrix (ECM) *(2)*. Motility can be gained upon activation of the epithelial-mesenchymal transition (EMT) program *(6)*. During EMT, epithelial cells gradually lose cell-cell contacts, progressively strengthen their adhesions to the ECM and increase their contractility, becoming motile. Concomitantly to EMT, cancer cells can also acquire the capacity to locally degrade the ECM using invadopodia *(7–10)*. Invadopodia are membrane protrusions enriched in matrix metalloproteinases (MMPs) that confer cancer cells with high proteolytic activity *(11, 12)* and importantly elevated metastatic potential *(13, 14)*. Since the EMT program is not a binary, nor a unidirectional switch, and since multiple EMT routes exist, distinct EMT trajectories may result in cancer clones with different levels of invasiveness *(15)*.

Recent 3D *in vitro* work on breast cancer showed that invasive collective strands are composed of cancer cells that differ on multiple invasive traits *(3, 16–20)*. For example, compared to follower cells, leader cells show increased contractility *(19)*, cell-ECM adhesion *(3, 16)*, ECM remodeling *(20)* and ECM degradation capacities *(18, 19)*. As a result, leader cells can enable the invasion of otherwise non-invasive follower cells, a phenomenon termed cooperative invasion *(21)*. Our recent work showed that leader cells largely reside in the G1 phase of the cell cycle, the phase of the cell cycle during which invadopodia-mediated ECM degradation is the highest *(22)*. These data suggest that during collective invasion, leader cells may preferentially assemble invadopodia. Although breakdown of the ECM is clearly required for collective invasion, the role of invadopodia-mediated ECM degradation in leader *vs.* follower cells is unclear.

While several studies have been published on cooperative invasion of cancer cells in 3D settings, the steps that may lead to it, and the effects it may have on metastasis were not explored yet.

In this study, we aimed to understand how cancer clones with differential invasive skills may cooperate during invasion and metastasis. We show that invasive clones can sort from and lead non-invasive clones into cooperative invasion and metastasis. Our study suggests that cooperativity between cancer cells may be an efficient mechanism for collective metastasis.

Results

4T1 cells, but not 67NR cells, invade into collagen I

To investigate how cancer clones with differential invasive skills cooperate during metastasis we utilized the syngeneic breast cancer cell lines 4T1 and 67NR *(23, 24)*. Upon orthotopic implantation in mice, both cell lines grow primary tumors, but only 4T1 cells metastasize *(25)*. We assessed the invasive capacities of 4T1 and 67NR cells in the spheroid invasion assay with high-density collagen I, which requires MMP-driven degradation of the matrix *(22)*. After 2 days, we found that the 4T1 cells exhibited robust invasion into the collagen I matrix, while 67NR cells did not invade (Fig. 1A, B). Treatment with the pan-MMP inhibitor GM6001 (Fig. 1A, B) and labeling of MMP-mediated collagen I cleavage (Fig. 1C) showed that the invasion of 4T1 cells into the matrix was MMP-dependent. Treatment with mitomycin C, which impairs cell division *(26)*, confirmed that the invasion of 4T1 cells was not due to cell proliferation (Fig. 1A, B and fig. S1). 4T1 cells are known to invade as collective strands, with presence of E-cadherin at cell-cell junctions *(27, 28)*. We confirmed that 4T1 cells expressed E-cadherin, while 67NR cells expressed N-cadherin (fig. S2A, B) *(27–29)*. Both 4T1 and 67NR cells lines expressed vimentin (fig. S2A).

Interestingly, on the EMT axis, this classifies the invasive 4T1 cells as epithelial/mesenchymal (E/M) and the non-invasive 67NR cells as mesenchymal. Further, in the 4T1 spheroids, we found E-cadherin to be enriched at the border of leader and follower cells, which verified that the integrity of E-cadherin-mediated cell-cell junctions was maintained following invasion (fig. S2C, D). Overall, these results demonstrated that 4T1 cells perform MMP-dependent collective invasion, while the 67NR cells do not invade into a dense collagen I matrix.

Invadopodia are membrane protrusions enriched in actin, actin-binding proteins- such as cortactin and Tks5- and MMPs *(11, 12)*. As invadopodia function results in focused ECM degradation, we hypothesized that invadopodia might play a role in the invasion of 4T1 cells. We also reasoned that the observed difference in the invasion capacities of 4T1 *vs.* 67NR cells might be explained, at least in part, by a disparity in their invadopodia function. To test this, we first analyzed the expression level of the key invadopodia components cortactin and Tks5 *(11)*. Both cell lines expressed cortactin and Tks5 (Fig. 1D). We next measured invadopodia function by culturing cells on top of fluorescently labeled gelatin, which allows visualization of degradation as holes in the matrix *(30)*. We found that 4T1 cells, but not 67NR cells, were able to degrade the gelatin layer (Fig. 1E, F). Puncta of co-localized Tks5, F-actin and degraded gelatin, indicative of functional invadopodia, were present in 4T1 cells (Fig. 1G). This suggest that the observed degradation holes were generated by invadopodia. To examine whether invadopodia also play a role in the invasion of 4T1 cells in spheroids, we labeled spheroids for F-actin, Tks5 and MMP-mediated collagen I cleavage. We identified functional invadopodia in leader cells (Fig. 1H). These observations established a link between invadopodia and collective invasion of 4T1 cells and suggest that leader cells may assemble invadopodia. Since invasion is a combination of invadopodia-mediated ECM degradation and motility *(31)*, we performed the scratch assay to investigate whether 67NR cells can migrate as efficiently as 4T1 cells. We tracked individual cells (Fig. 1I, J; movie S1 and movie S2) and found that while the instantaneous speed of 67NR cells is higher than that of 4T1 cells (Fig. 1K), 4T1 cells were significantly more persistent than 67NR cells (Fig. 1L).
In summary, we showed that the 4T1/67NR pair is a suitable tool to investigate how cancer clones with differential invasive skills cooperate during invasion.

Differential persistence drives cell sorting between 4T1 and 67NR cells

Based on the differential adhesion hypothesis *(32)*, we reasoned that a mixture of 4T1 and 67NR cells would sort from each other, with N-cadherin expressing 67NR cells surrounding E-cadherin expressing 4T1 cells. To test this hypothesis, we generated a 67NR-GFP cell line (expressing cytoplasmic GFP) and a 4T1-mScarlet cell line (expressing cytoplasmic mScarlet). These cells were used to form mixed spheroids at a 1:50 ratio of 4T1-mScarlet:67NR-GFP cells, to account for the difference in their proliferation rate over the course of the spheroid invasion assay (fig. S3A, B). To test if cells sort, we embedded the mixed spheroids in collagen I and performed longitudinal imaging (Fig. 2A and fig. S3C). We noticed that 67NR and 4T1 cells were sorted from each other starting day 3 and before invasion occurred, which was easily visible in individual optical slices (movie S3) and when cell coordinates were plotted (Fig. 2B). To quantify cell sorting, we calculated the relative distance from each cell to the spheroid center, a metric we named distance index (DI), such that a value of 0 marks the cell at the spheroid center and a value of 1 marks the cell at the spheroid-collagen I interface (Fig. 2C). At day 3 after embedding the spheroids in collagen I, we found that the DI of 4T1 cells was increasing over time and significantly higher compared to 67NR cells (Fig. 2D and fig. S3D). These data revealed that, over the course

of 3 days, cells reorganized from a homogenous distribution within spheroids into two compartments: one compartment in the spheroid edge, at the interface with collagen I, containing 4T1 cells, and one compartment in the spheroid core, containing 67NR cells. In addition, these results indicated that cell sorting of 4T1 and 67NR cells preceded invasion (fig. S3E).

Spheroids of 4T1 cells have been shown to contain laminin, collagen I and fibronectin, which accumulate in between cells *(33)*, suggesting that 3D cell motility within the spheroid may require MMPs. To test the link between motility, MMPs and cell sorting, we treated spheroids with an inhibitor of cell contractility (ROCK inhibitor, Y-27632) or a pan-MMP inhibitor, GM6001. We found that both treatments blocked cell sorting (Fig. 2E, F). We then performed time-lapse imaging of mixed spheroids, treated with DMSO control or GM6001 to block cell motility in spheroids. We tracked individual cells within the spheroid (movies S4 and S5) and for each cell, calculated the difference between the initial and final distance indices (ΔDI), such that a positive ΔDI indicates cell movement towards the spheroid edge, and a negative ΔDI indicates movement towards the spheroid center (Fig. 2G-I). A null ΔDI may indicate no movement or cell movement within a compartment. We classified each cell based on their initial position as "edge" or "core", and defined the edge compartment as the two cell layers closest to the spheroid-collagen interface (30 µm-wide elliptical ring; Fig. 2G). We next confirmed that the percentage of tracked cells that switched between compartments during the duration of the timelapse was negligible for all but the 4T1 cells initially located in the core (fig. S4A). For 4T1 cells, we found that the ΔDI was significantly higher for cells whose initial position was in the spheroid core compared to cells whose initial position was in the spheroid edge (Fig. 2 H, I). This indicates that 4T1 cells moved from the spheroid core towards the spheroid edge. In contrast, 4T1 cells located at the spheroid edge had a ΔDI close to zero (Fig. 2I), suggesting that 4T1 cells that reached the spheroid edge either moved within the compartment, or stopped moving. In 67NR cells, ΔDIs were minimal for all cells, regardless of their initial position (Fig. 2I). To quantitatively address motility characteristics of both cell types, we converted the coordinates of cell trajectories to polar coordinate system, calculated the mean square displacement (MSD) in control conditions and determined that they fit to the persistent random walk model (PRW) (Fig. 2J). Using the PRW, we then extracted the instantaneous speeds and persistence lengths for all cells (Fig. 2K, L). Both cell types had similar speeds independent of the compartment. Interestingly, speeds increased from 4.17 and 4.95 micron/hour in the core, to 8.29 and 8.55 microns/hour in the edge compartment. Instantaneous speeds in GM6001 condition were similar independent of cell type or location, and ranged from 3.9 to 4.3 microns/hour. In contrast, persistence length was largely dependent on cell type and not compartment. While values for 67NR ranged from 2.41 microns in the core to 1.71 microns in the edge compartment, in 4T1 cells, persistence was 4.8 microns in the core and 5.5 microns in the edge compartment. Importantly, MMP inhibition significantly reduced the persistence of all cells (Fig. 2L), and impaired the movement of 4T1 cells from the core to the edge (Fig. 2I). We confirmed that the spheroid growth was similar in the GM6001 and DMSO conditions, suggesting that the loss of cell sorting was independent from cell proliferation (fig. S4B). Taken together, these results indicate that while the instantaneous speed of 67NR cells is similar to 4T1 cells, they demonstrate lower persistence lengths (Fig. 2L). In addition, 4T1 cells, but not 67NR cells, move from the core to the edge compartment and remain at the spheroid edge, all of which contributes to cell sorting between the two cell types. In summary, we showed that differential persistence drives cell sorting between 4T1 and 67NR cells.

An adhesive ECM interface is required for maintenance of cell sorting

Since cell sorting occurred at day 3 post collagen-embedding (Fig. 2A, D), and that 4T1 cells actively accumulated at the spheroid edge (Fig. 2I), we reasoned that the interaction of 4T1 cells with the ECM may be critical for maintaining cell sorting. To test this, we placed mixed spheroids in a non-adherent matrix of agarose. At day 3 and 4, the DI was similar for both 4T1 cells and 67NR cells, demonstrating that cells embedded in agarose did not sort (Fig. 3A, B). We also confirmed that the spheroid area was similar in the collagen I and agarose conditions, indicating that the loss of cell sorting was independent from cell proliferation (fig. S4C). This lack of cell sorting could be due to the failure of 4T1 cells to remain at the spheroid edge when the adhesive ECM is absent. To test this in real-time, we performed time-lapse imaging of mixed spheroids embedded in agarose and tracked individual 4T1 cells (Fig. 3C; movie S6 and S7). We found that the average ΔDI for cells starting in the edge compartment was negative, and close to zero for cells starting in the core compartment (Fig. 3D). This indicates that 4T1 cells move from the spheroid edge inwards (movie S6), or move within the core compartment. We also observed core cells entering and subsequently leaving the edge compartment (movie S7).

We then hypothesized that, compared to 67NR cells, 4T1 cells preferentially adhere to the ECM. To compare the adhesive properties of 4T1 and 67NR cells to collagen I, we developed a 2D cell-ECM competition assay in which both cell types are plated on top of adhesive gelatin islands that are surrounded by a non-adhesive poly-L-lysine coating and initially devoid of cells (Fig. 3E). After 24 h, we scored the number of 4T1 and 67NR cells that migrated off the gelatin islands. We found that, of all the cells that moved off the gelatin, 85% of them were 67NR cells (Fig. 3F). In time-lapse movies, we observed that 4T1 cells that crossed the gelatin/poly-L-lysine interface migrated back to the gelatin layer (movie S8). We wondered whether this could be explained by 4T1 cells having a higher adhesion strength to gelatin than 67NR cells. To test this, we measured the contact angle of cells plated on gelatin or poly-L-lysine (Fig. 3G). The cell-matrix contact angle was previously shown to increase with the adhesion strength *(34)*. We found that while both cell types had similar contact angle when plated on gelatin (Fig. 3H), 4T1 cells plated on poly-L-lysine had a significantly lower contact angle compared to 67NR cells (Fig. 3H), indicating that, compared to 67NR cells, 4T1 cells are more sensitive to the presence of ECM. This result is in line with the observation that the FAK protein level is higher in 4T1 cells than in 67NR cells (fig. S5A). By analyzing cell-cell contacts between 4T1 and 67NR cells plated on gelatin, we found that the percentage of homotypic contacts was similar at the time of plating (0 h) and at 24 h post plating (fig. S5 B, C). This proved that 4T1 and 67NR cells did not sort in 2D, suggesting that the differential adhesion hypothesis is not the main driver for cell sorting in our system. Moreover, this also emphasized the need for an ECM interface for cell sorting to occur.

4T1 cells lead 67NR cells in an MMP-dependent cooperative invasion

Following sorting of 4T1 and 67NR cells in spheroids at day 3 and 4, invasion occurred at day 5 and 6 (Fig. 2A and Fig. 4A; fig. S3C). One mechanism by which cancer cells can invade collectively is cooperation: invasive leader cells create microtracks inside the ECM, followed by non-invasive cells *(18–21)*. Since 4T1 and 67NR cells display differential invasive skills, we reasoned that 4T1 cells could enable the cooperative invasion of the non-invasive 67NR cells. To test this hypothesis, we analyzed the mixed spheroids at day 6 post embedding. We observed that the non-invasive 67NR cells entered the collagen I matrix (Fig. 4A). Accordingly, we found that, compared to spheroids made of a single cell line, mixed spheroids had an increased number of strands per spheroid (Fig. 4B), approximately one third of which contained 67NR cells (Fig. 4C). Moreover, in mixed spheroids, we

observed that the majority of strands was led by 4T1 cells (Fig. 4D). Importantly, according to the MMP-dependency of 4T1 cells for invasion, GM6001 treatment blocked the cooperative invasion of 4T1 and 67NR cells (Fig. 4A-C). During cooperative invasion, cell sorting between 4T1 and 67NR cells was maintained in the invasive strands as well as within the spheroid (Fig. 2E-G). Altogether, these findings demonstrate that an MMP-dependent cooperative invasion occurs between the two cell lines, with 4T1 cells assuming the leader position.

Based on our results so far, we proposed that the 4T1-mediated ECM degradation is required for 67NR cells to enter the collagen I matrix. Following this proposition, we assumed that, for cooperative invasion to occur, 4T1 cells need to be in the collagen I matrix in order to degrade it. To confirm our assumption, we embedded 67NR spheroids in collagen I containing 4T1 cells. Similarly to our observations in mixed spheroids, we found that upon addition of 4T1 cells into collagen I, 67NR cells invaded into the matrix in an MMP-dependent manner (fig. S6A, B). To exclude the possibility that soluble MMPs released by 4T1 cells facilitated the invasion of 67NR cells into the collagen I matrix, we cultured spheroids of 67NR cells with conditioned medium from 4T1 cells. We found that providing conditioned medium from 4T1 cells to 67NR cells was not sufficient for them to invade into the collagen I matrix (fig. S6C, D). In mixed spheroids, we identified microtracks inside the collagen I matrix, filled with 4T1 cells leading and 67NR cells following (fig. S6E). Overall, our data suggest that 4T1 cells degrade the collagen I matrix and lead 67NR cells into cooperative invasion.

Heterotypic cooperative invasion between cancer-associated fibroblasts and epithelial cancer cells has been shown to involve the formation of heterotypic N-cadherin/E-cadherin adhesions *(35)*. We did not detect heterotypic E-cadherin/N-cadherin adhesions between 4T1 and 67NR cells (fig. S7A-C), suggesting that the cooperative invasion between these cells does not require N-cadherin/E-cadherin junctions.

Cells with invadopodia lead cells without invadopodia in cooperative invasion

Since 4T1-mediated ECM degradation seemed to be required for cooperative invasion, we reasoned that invadopodia assembled by 4T1 cells could be implicated. To rigorously confirm that invadopodia function is involved in cooperative invasion of cancer cells, we eliminated invadopodia in 4T1-mScarlet cells using Tks5 knockdown (4T1-KD) *(13)*, and established a 4T1-shControl (4T1-CTL) cell line (Fig. 5A). We confirmed that 4T1-KD cells lost their invasive capacities in the gelatin degradation assay (Fig. 5B, C) as well as in the spheroid invasion assay (Fig. 5D, E). We also verified that 4T1-CTL and 4T1-KD cell lines still expressed E-cadherin (Fig. 5A). We then performed the spheroid invasion assay for an equal mixture of 4T1-CTL and 4T1-KD cells. At 2 days after embedding spheroids, we found that the non-invasive 4T1-KD cells had entered the collagen matrix (Fig. 5D). Compared to 4T1-KD spheroids, mixed spheroids had an increased number of strands (Fig. 5E), most of which contained KD cells (Fig. 5F) and were led by 4T1-CTL cells (Fig. 5G). Similar results were obtained when invadopodia were eliminated in the human breast cancer cell line MDA-MB-231 (fig. S8A-G). To further test the importance of invadopodia in cooperative invasion of cancer cells, we performed the spheroid invasion assay for a mixture of 4T1-KD and 67NR-GFP cells. As expected for a mixture of clones without invadopodia, we did not observe invasive strands (Fig. 5H, I). Overall, these results demonstrate that cells with invadopodia are required to lead cooperative invasion, and that follower cells can lack invadopodia.

We did not observe cell sorting between 4T1-CTL and 4T1-KD cells (fig. S9A), but we observed cell sorting between 4T1-KD and 67NR-GFP cells (fig. S9B). These findings indicate that invadopodia are not required for cell sorting. Since 4T1-CTL and 4T1-KD cells display similar motility skills and cell-ECM adhesion properties (fig. S9C, D), these observations also strengthen the requirement for differential persistence and differential cell-ECM sensitivity for cell sorting to occur. In accordance with this statement, we did not observe cell sorting between 4T1-mScarlet and 4T1 cells (fig. S9E, F).

Cells with invadopodia and without invadopodia perform cooperative metastasis

Finally, we wanted to investigate whether cells with invadopodia could enable metastasis of cells without invadopodia, a processed we named cooperative metastasis. To test this, we performed the lung clonogenic assay for single or a mixture of 4T1-CTL and 4T1-KD cell lines. To determine whether a colony is made of 4T1-CTL or 4T1-KD cells, we leveraged the fact that 4T1-KD cells are resistant to puromycin and geneticin, while 4T1-CTL cells are resistant to puromycin only. We confirmed that 4T1-KD cells were not capable of lung metastasis compared to 4T1-CTL cells (Fig. 5J). Surprisingly, when 4T1-CTL and 4T1-KD cells were co-injected, we found that 4T1-KD cells were capable of lung metastasis (Fig. 5J), suggesting that cooperative metastasis occurred.

Discussion

In this study, we show that invasive clones can sort from, and lead non-invasive clones during cooperative invasion and metastasis. By examining cell movements in spheroids, we demonstrate that differential persistence and ECM affinity drive cell sorting between clones. Through invadopodia removal, by silencing Tks5, we demonstrate that cells with invadopodia lead cells without invadopodia in cooperative invasion and enable their metastasis.

We confirm previous observations that the invasive 4T1 cells are hybrid epithelial/mesenchymal, while the non-invasive 67NR cells are mesenchymal (*27–29)*. It was previously shown that the Twist expression, necessary for invadopodia *(8)*, is present in 4T1 cells, but not 67NR cells *(36)*. Hence, Twist-mediated EMT could be responsible for the differences in invasion skills between 4T1 and 67NR cells *(36)*. Since 4T1 cells, but not 67NR cells, assemble functional invadopodia, it seems that specific invadopodia-granting EMT trajectory, rather than its completion is required for invadopodia emergence. Also, completion of EMT does not necessarily grant cancer cells with invadopodia. Our results are in line with the recent evidence that hybrid E/M cells can metastasize, sometimes even more efficiently than M cells *(37–39)*.

Despite expressing the core invadopodia components cortactin and Tks5, 67NR cells fail to degrade the matrix. However, 67NR cells lack active MMP-2 and MMP-9, likely due to MMP-14 not being functional and/or not being delivered to the plasma membrane of these cells *(40, 41)*.

For the first time, we here uncover the role of differential persistence and cell-ECM sensitivity in establishment of cell sorting in cancer. Classical studies on cell sorting during development showed that cell sorting relies on differential strength of cell-cell adhesions *(32)*, or on differences in contractility *(42)*. In contradiction to these views, we show that 4T1 and 67NR cells did not sort on a 2D gelatin layer or when placed in a 3D agarose matrix. The importance of differential motility in sorting was previously suggested during tissue patterning *(43)*, and in engineered breast tubules, where it was shown that more directional epithelial cells accumulate at the tissue edge *(44)*. During self-organization of mammary ducts, binary cell-ECM interaction state (ON or OFF) was reported to regulate cell sorting *(34)*. Similarly to our observations, Pawlizak *et al.* recently demonstrated that sorting of

breast cell lines expressing E-, N- or P-cadherin could not be explained by the differential adhesion hypothesis *(45)*. Interestingly, the authors proposed that motility could be responsible for cell sorting.

We find that sorting can precede cooperative invasion, resulting in invasive cells accumulating at the spheroid-ECM interface and leading invasion strands. This emphasizes the importance of studying the mechanisms regulating the spatial organization of leader and follower cells. The accumulation of leader cells at the spheroid-matrix interface, rather than follower cells, may enhance the speed and efficiency of their cooperative invasion. Supporting these views, a recent study demonstrated that cell sorting precedes the basal extrusion of mammary epithelial cells *(46)*.

Since the discovery of cooperative invasion, significant work has been carried out to uncover the mechanisms by which heterogeneous breast cancer cell populations interact and mobilize collectively. Our work suggests that invadopodia activity is a determinant of the leader cell phenotype. We previously showed that the G1 phase of the cell cycle is also a determinant of the leader cell identity *(22)*. Consistent with this present work, we had also proved that invadopodia are enriched in the G1 phase of the cell cycle *(22)*. A different study revealed that cells leading invasion strands possess higher intracellular energy compared to follower cells *(17)*. Altogether, it seems that the G1 phase of the cell cycle, intracellular energy and invadopodia function are determinants of the leader cell identity. However, the interplay between the cell cycle, intracellular energy and invadopodia function yet needs to be investigated in the context of the emergence of leaders and followers within cell populations.

In summary, our study suggests that cooperativity between cancer clones may be an efficient mechanism for collective metastasis. Specifically, we demonstrate that invadopodia enable cooperative metastasis and allow non-invasive cells to metastasize. To our knowledge, our work constitutes the first evidence for cooperative metastasis, which may be more dangerous than the metastasis of singletons. We propose that targeting invadopodia could be a potent strategy to inhibit metastasis of both individually *(13, 14)*, as well as collectively, invading cells.

Materials and Methods

Ethics statement

All experiments on mice (Mus musculus) were conducted in accordance with the NIH regulations and approved by the Temple University IACUC protocol number 4766.

Fabrication of the spheroid imaging devices (SIDs)

Spheroid imaging devices (SIDs) were fabricated as previously described *(47)*. Briefly, SIDs were made by bounding poly(dimethylsiloxane) (PDMS) rings to glass bottom dishes (MatTek Corporation). Each PDMS ring measures 17.5 mm in diameter and contains three 5.5 mm-diameter holes.

Gelatin coating of 6-well plates for cell culture

6-well plates were coated with gelatin as previously described *(48)*. Briefly, each well was coated with a 2.5% gelatin solution for 10 min followed by treatment with 0.5% glutaraldehyde (Sigma-Aldrich) for 10 min, on ice, and an extra 30 min at room temperature. Plates were sterilized by 70% ethanol and then 50 U/mL penicillin - 50 µg/mL streptomycin treatment.

Plasmids

pmScarlet-C1 was a gift from Dorus Gadella (Addgene plasmid # 85042). pEGFP-puro was a gift from Michael McVoy (Addgene plasmid # 45561).

Cell culture

The isogenic murine breast cancer cell lines 4T1 and 67NR were a gift from Fred R. Miller at the Karmanos Cancer Center. The human breast cancer cell line MDA-MB-231 (HTB-26) was obtained from the American Type Culture Collection. The MDA-MB-231-Dendra2-Tks5 KD cell line was described previously *(13)*. All cells were cultured in Dulbecco's modified eagle medium [4.5 g/L D-glucose, L-glutamine] (DMEM, Gibco), supplemented with 10% fetal bovine serum (FBS, Atlanta Biologicals) and 50 U/mL penicillin - 50 µg/mL streptomycin (Gibco). Cell cultures were maintained at 37 °C and 5% CO_2 for a maximum of 60 days.

The 4T1-mScarlet and 67NR-GFP cell lines were generated by transfection using a 1:4 ratio of plasmid DNA:FugeneHD reagent (Promega), according to the manufacturer's instructions, followed by selection with 500 µg/mL geneticin (Fisher BioReagents) and 3 µg/mL puromycin (MP Biomedicals), respectively. The MDA-MB-231-mScarlet cell line was generated by electroporation (Lonza) of the pmScarlet-C1 plasmid, according to the manufacturer's instructions, and selection with 500 µg/ml geneticin. After two weeks of drug selection, cells were sorted with a gating strategy to obtain a high expression level of the fluorescent protein mScarlet or Dendra2 (BD FACSAriaIIµ, BD Biosciences).

4T1-mScarlet-mTks5 KD, 4T1-shCTL and MDA-MB-231-mScarlet-shCTL cell lines were generated by lentiviral transduction (see "Lentivirus transduction" section).

Lentivirus transduction

The Tks5 knockdown cell line (KD) and the knockdown control cell line (CTL) were generated by transduction of the 4T1-mScarlet and the 4T1/MDA-MB-231-mScarlet cell lines, respectively, with lentiviral particles (3 viral particles/cell) containing shRNA targeting mTks5 (KD) or non-targeting shRNA (CTL) in the pLKO.1-puro vector (MISSION library, Sigma-Aldrich), and selection with 2 µg/mL puromycin 3 days after infection.

2D proliferation assay and analysis

Crystal violet staining was used to assess the effect of mitomycin C on the proliferation of the 4T1 cell line. Briefly, 4T1 cells were seeded in a 6-well plate and the next day, the culture medium was replaced with culture medium containing 0.5 µg/mL Mitomycin C (resuspended in DMSO, Cayman Chemical). After 2 days, cells were washed with cold PBS, fixed with ice-cold 100% methanol for 10 min and stained with 0.5% crystal violet solution in 25% methanol for 10 min at room temperature. Excess dye was removed by several washes with tap water and the plate was air dried overnight at room temperature. The dye was solubilized using 100% methanol for 20 min and the optical density was read on a plate reader at 570 nm. The optical density at 570 nm for mitomycin C-treated cells was reported to the optical density at 570 nm for DMSO-treated cells.

2D gelatin degradation assay and immunofluorescence labeling

Gelatin was fluorescently labeled and 35 mm glass bottom dishes (MatTek Corporation) were coated with fluorescently labeled gelatin as previously described *(30)*. 400,000 (4T1/67NR) or 3000,000 (MDA-MB-231) cells were plated per dish and cells were fixed 18 h later with 4% paraformaldehyde (Alfa Aesar) for 10 min, permeabilized with 0.1% Triton X-100 (Calbiochem) for 5 min, blocked with 1% FBS/1% BSA (Sigma-Aldrich) in PBS (Gibco) for 3 h, incubated with anti Tks5 antibody (Millipore, MABT336) for 2 h then with secondary antibody and Alexa Fluor 633 Phalloidin (Invitrogen) for 1 h.

Image acquisition and quantification of the gelatin degradation assay

Samples were imaged on a laser scanning confocal microscope (FV1200, Olympus) using a 60X objective (UPLSAPO60XS | 1.35 NA, Olympus). Stacks were collected at 1 µm z-step. To quantify matrix degradation, images were processed using a custom macro in Fiji. Briefly, slices from the stack were z-projected using the *Max Intensity* method, followed by thresholding of the signal in the gelatin channel, using the *Automatic Threshold* algorithm, and measuring the area of degradation spots using the *Particle Analysis* tool. To account for the differences in the cell density across fields of view, the total area of degradation in a field of view was divided by the total number of cell present in this field of view. Cells were counted using the F-actin channel.

Scratch assay

6-well plates were coated with 50 µg/ml poly-L-lysine (Sigma-Aldrich) for 20 min and let to air dry. Cells were plated and grown to confluency before a 10 µl pipet tip was used to create a cross-shaped wound across the monolayer. Samples were imaged on a widefield microscope (IX-81, Olympus) equipped with an LED lamp (Excelitas Technologies), an Orca 16-bit charge-coupled device camera (Hamamatsu), an automated z-drift compensation IX3-ZDC (Olympus), an automated stage (Prior Scientific), an environmental chamber (Live Cell Instrument) and using a 10X objective (MPlanFL N 10X | 0.3 NA, Olympus). Cell motility was recorded at a 10 min interval over 48 hours. Manual cell tracking was performed using the TrackMate plugin through Fiji *(49)*. The track number, the spot coordinates and the frame number were exported. Computation of the velocity and persistence were done using a custom made Matlab code (available upon request).

Generation of gelatin islands and 2D cell-ECM competition assay

To generate gelatin islands, we utilized the PDMS rings described previously (see "Fabrication of the spheroid imaging devices (SIDs)" section). Briefly, 35 mm glass bottom dishes (MatTek Corporation) were coated with 50 µg/ml poly-L-lysine (Sigma-Aldrich) for

20 min and let to air dry. Then, PDMS rings were gently placed on top of the glass and sealed by gently pressing down. Next, each 5.5 mm-diameter hole was coated with fluorescently labeled gelatin as previously described *(30)* (see "2D gelatin degradation assay and fluorescence labeling" section). 4T1-mScarlet and 67NR-GFP cells were plated in each hole at a 1 to 1 ratio. After 1 h, the PDMS inserts were gently peeled off the glass and medium was added to the dishes. Finally, cells were fixed 24 h later with 4% paraformaldehyde (Alfa Aesar) for 10 min.

Image acquisition and quantification of the 2D cell-ECM competition assay and 2D cell sorting

Samples were imaged on a widefield microscope (Eclipse Ti2-E, Nikon) equipped with a pco.panda sCMOS camera (PCO) and using a 10X objective (CFI Plan Fluor 10X | 0.3 NA, Nikon). Large 6x6 tiles were acquired to cover a gelatin island. Live cells were imaged every 10 min and using an environmental chamber (Tokai Hit). To quantify the 2D cell-ECM competition assay we counted the number of 4T1 and 67NR cells that migrated off the gelatin island. To quantify cell sorting in 2D we only utilized regions coated with gelatin and we counted the number of homotypic neighbors.

Image acquisition and quantification of the cell-ECM contact angle

Measurement of the contact angle was performed as previously described *(34)*. Briefly, 35 mm glass bottom dishes (MatTek Corporation) were coated with fluorescently labeled gelatin as previously described *(30)* or with 50 µg/ml poly-L-lysine (Sigma-Aldrich) for 20 min and let to air dry. Cells were let to adhere for 5 h before imaging. Single cells were screened for an absence of interaction with nearby cells and were imaged on a laser scanning confocal microscope (FV1200, Olympus) using a 60X objective (UPLSAPO60XS | 1.35 NA, Olympus) equipped with an environmental chamber (Live Cell instrument) and with a 1 µm z-step. Using *Orthogonal Views*, we measured the angle between the ECM and the main body of the cell: the contact angle.

3D spheroid invasion assay

For 4T1 and 67NR cell lines, 3D spheroids were generated by the hanging drop method. 3,000 cells per 40 µl drop containing 4.8 mg/mL methylcellulose (Sigma-Aldrich), 20 µg/mL Nutragen (Advanced Biomatrix), were placed on the lid of tissue culture dishes. The lids were carefully turned and placed on the bottom reservoir of the dishes filled with PBS to prevent evaporation. Alternatively, for MDA-MB-231 cell lines, 3D spheroids were generated in a 96-well V-bottom dish coated with 0.5% poly(2-hydroxyethyl methacrylate) (Sigma-Aldrich) in ethanol. Then, 5,000 cells in 50 µl of medium were distributed to each well and the plate was centrifuged for 20 min at 1,000 x g and at 4°C. Finally, 50 µl of Matrigel (Corning) was added to each well at a final concentration of 2.5%. The spheroids formed over 3 days at 37 °C and 5% CO_2. The fully formed spheroids were embedded in 30 µl of 5 mg/mL rat tail Collagen I (Corning, alternate gelation protocol) and distributed to the SIDs. Collagen I was polymerized at 37 ºC for 30 min and then culture medium was added to the dishes. For drug treatments, cell culture medium containing 25 µM GM6001 (resuspended in DMSO, Cayman Chemical), 10 µM Y-27632 (resuspended in DMSO, Cayman Chemical) or 0.1% DMSO was used.

For the condition in which 4T1-mScarlet cells surround the 67NR-GFP spheroids, 4T1-mScarlet cells were added to the collagen mix containing the 67NR-GFP spheroids at 10^6 cells/mL before polymerization of the collagen.

For the condition in which conditioned medium was used, 4T1-mScarlet cells were seeded onto a gelatin-coated 6-well plate, at $2x10^6$ cells/well. 2 mL of complete DMEM were used

per well and the embedded 67NR-GFP spheroids were cultured, from day 0, using the conditioned medium from the 4T1-mScarlet cells plated onto gelatin. Every two days, the conditioned medium was replaced.
Collagen was labeled as previously described *(50)*, using 2 µg/ml of 405 succinimidyl ester (biotium).

Immunofluorescence labeling of spheroids

Immunofluorescence labeling was performed as previously described *(47)*. Briefly, the embedded spheroids were simultaneously fixed and permeabilized in 4% paraformaldehyde and 0.5% Triton X-100 in PBS for 5 min, further fixed in 4% paraformaldehyde in PBS for 20 min and blocked in 1% FBS/1% BSA in PBS at 4 ºC for 24 h on a shaker. The embedded spheroids were then incubated with the anti-collagen I ¾ (immunoGlobe, 0207-050), anti E-cadherin (Invitrogen, 13-1900), anti N-cadherin (BD Transduction Laboratories, 610920) and anti Tks5 (Millipore, MABT336) overnight at 4 ºC and with secondary antibodies and Alexa Fluor 633 Phalloidin (Invitrogen) for 1 h on a shaker.

Image acquisition, processing and analysis of fixed spheroids

To quantify the <u>total spheroid area</u>, the DAPI-labeled spheroids were imaged on a laser scanning confocal microscope (FV1200, Olympus) using a 10X objective (UPLXAPO10X | 0.4 NA, Olympus) and with a 5 µm z-step. The images were processed using a custom macro in Fiji. Briefly, slices were z-projected using the *Max Intensity* method and the nuclei were selected using the *Automatic Threshold* algorithm from Fiji. Then, the *Particle Analysis* tool was used to measure the total area of nuclei.
To quantify the <u>E-cadherin signal</u>, the immunolabeled spheroids were imaged on a laser scanning confocal microscope (FV1200, Olympus) using a 10X objective (UPLXAPO10X | 0.4 NA, Olympus) or a 30X objective (UPLSAPO30XSIR | 1.05 NA, Olympus) and with a 3 µm z-step. The images were processed manually in Fiji. Briefly, slices of interest were z-projected using the *Max Intensity* method and strands or single cells were identified. For the relative junction/cytosol ratio: a 10 µm-long line was drawn across and centered at the junction between two cells within a strand. The gray value along the line was measured for the E-cadherin and F-actin channel using the *Plot Profile* tool. The gray value at 0 and 5 µm were defined as the "cytosol" and "junction" signal, respectively. Since it was reported that leader cells can exhibit a more mesenchymal-like phenotype than follower cells *(51)*, we distinguished leader cell-follower cell (L-F) junctions from follower cell-follower cell (F-F) junctions.
To quantify <u>cell sorting</u>, endogenously labeled spheroids were imaged on a laser scanning confocal microscope (FV1200, Olympus) using a 10X objective (UPLXAPO10X | 0.4 NA, Olympus) and with a 5 µm z-step. The images were processed using a custom macro in Fiji. Since maximum projection of the z-slices introduces artefacts in the positions of cells, regarding the spheroid edge *vs.* core compartments, we utilized the median slice of the z-stack only. Briefly, the median slice was extracted from the z-stack and the spheroid core was selected in the brightfield channel using the *Automatic Threshold* algorithm from Fiji. Then, using the *Fit Ellipse* and *Centroid* options in *Measurements*, the coordinates of the spheroid core center and the major axis of the spheroid core were extracted. Finally, the *Multi-point* tool was used to record the coordinates of GFP+ and mScarlet+ cells. Cell sorting was quantified as the distance from the spheroid center to the cell (d in Fig. 2C) over the semi major axis of the spheroid (a in Fig. 2C). Alternatively, for mixed spheroids that contained non-labeled cells, like 4T1-shCTL (Fig. 5) or 4T1 cells (fig. S7), DAPI staining was used to measure the cells coordinate.

Live imaging of spheroids and image processing

To observe cell sorting in spheroids imaged daily, endogenously labeled spheroids were imaged on a laser scanning confocal microscope (FV1200, Olympus) using a 10X objective (UPLXAPO10X | 0.4 NA, Olympus) equipped with an environmental chamber (Live Cell instrument) and with a 15 µm z-step. To quantify cell sorting, the images were processed as described in the section "Image acquisition, processing and analysis of fixed spheroids".

To observe cell motility in spheroids, time-lapse imaging was performed on a laser scanning confocal microscope (Olympus FV1200) using a 10X objective (UPLXAPO10X | 0.4 NA, Olympus) equipped with an environmental chamber (Live Cell instrument) and an automated stage (Prior Scientific). Invasion was recorded at 10- or 20-min intervals over 44 hours, with a 15 µm z-step. The images were processed in Fiji. Since visualization of cells in the spheroid internal compartment is limited for the deepest slices, and since cells visualized in the shallowest slices are at the spheroid interface compartment, only in-between slices, where both cells in the internal compartment and at the interface compartment of the spheroid are visible, were used for tracking. Cell tracking was performed using the TrackMate plugin through Fiji *(49)*. Spot detection was done using the LoG detector with median filtering and subpixel localization. Then, the linear motion LAP tracker was used to link spots. Tracks were filtered based on the number of spots in the track with a ≥ 5 spots/track cutoff. Tracks were visually validated and corrected if needed, using the TrackScheme tool. Finally, gaps in tracks were closed by introducing new spots. The new spots position was calculated using linear interpolation. The track number, the spot coordinates and the frame number were exported. Computation of the distance index was done using a custom made Matlab code (available upon request).

Mean-squared displacement analysis of cell tracks. Coordinates of individual cell trajectories were transformed from the Cartesian {x,y} to {r,θ} polar coordinate system, and their mean-squared-displacements (MSD) were calculated in the radial and angular directions. The radial MSD (r(t)) is then fit to the persistent random walk (PRW) model *(52)*, described by

$$\langle r^2(t)\rangle = 2SL_p[t - \frac{L_p}{S}\left(1 - e^{-\frac{St}{L_p}}\right)]$$

where the brackets denote averages over different cell tracks. Here, S denotes the velocity of a cell, and L_p denotes the persistence length of a cell. Cell tracks were also classified into two groups, namely edge or core cells. It is important to note that at short times, PRW model exhibits ballistic ($\sim t^2$). behavior, whereas at long times it is diffusive ($\sim t$).

Western blot assay

Cells grown to 80% confluency were harvested in ice-cold RIPA lysis buffer (Teknova), supplemented with protease inhibitors (complete cocktail, Roche) and phosphatase inhibitors (Halt cocktail, Sigma-Aldrich). SDS-PAGE was performed with 20 µg protein per sample, transferred to a polyvinylidene difluoride membrane (Immobilon), blocked with 5% BSA/TBST for 3 h at room temperature and incubated with anti-β-actin (Santa Cruz Biotechnology, sc-47778), anti-cortactin (Abcam, ab33333), anti-E-cadherin (BD Transduction Laboratories, 610181), anti-FAK (Santa Cruz Biotechnology, sc-271126), anti-N-cadherin (BD Transduction Laboratories, 610920) and anti-Tks5 (Millipore, MABT336) antibodies diluted in 5% BSA/TBST overnight at 4 ºC. The membranes were then incubated with HRP conjugated anti-mouse or anti-rabbit IgG (Cell Signaling Technologies) antibodies diluted in 5% non-fat milk/TBST for 1 h at room temperature and

proteins were visualized using chemiluminescence detection reagents (WesternBright, Advansta) and blot scanner (C-DiGit, LI-COR).

Lung clonogenic assay

The lung clonogenic assay was performed as previously described *(53)*. Briefly, 200,000 cells were suspended in 100 µl of 20% collagen I in PBS and injected orthotopically into the mammary fat pad of 7-week old female Balb/cJ mice. After 14–20 days, when the tumor diameter reached 8–12 mm, the animals were sacrificed and the lungs harvested. The lungs were minced, digested in a collagenase type IV/elastase cocktail (Worthington Biochemical) and filtered. Then, the cell suspension from each lung was plated onto 2 tissue culture plates and incubated with a combination of 6-thioguanine (Cayman Chemicals) and puromycin, for growth of 4T1-shControl or 4T1-mScarlet-mTks5 KD cells; or with a combination of 6-thioguanine, puromycin and geneticin for growth of 4T1-mScarlet-mTks5 KD cells only. After 14 days at 37 °C and 5% CO_2, the colonies were stained using 0.03% (w/v) methylene blue (Sigma-Aldrich) and counted.

Statistical analyses

The RStudio software was used to perform all statistical analysis. The distribution of each data set was analyzed, and the Shapiro-Wilk test was performed to test for normality. For normally distributed data sets, the F test was performed to compare the variances of two data sets. Based on the results from the F test, a Welch two sample t-test or a two sample t-test was done to compare the means of the two data sets. For non-normally distributed data sets a Wilcoxon rank sum test was performed to compare the two data sets. Except notified otherwise, all tests were performed using unpaired and two-sided criteria. Statistical significance was defined as *$p<0.05$, **$p<0.01$, and ***$p<0.001$. Additional information on the metrics and statistics can be found in the Table S1.

References

1. Howlader N, Noone AM, Krapcho M, Miller D, Brest A, Yu M, Ruhl J, Tatalovich Z, Mariotto A, Lewis DR, Chen HS, Feuer EJ, Cronin KA. SEER Cancer Statistics Review, 1975-2017, based on November 2019 SEER data submission [Internet]. National Cancer Institute. Bethesda, MD. 2020.
2. Vanharanta Sakari, Massagué Joan. Origins of Metastatic Traits. Cancer Cell. 2013 Oct;24(4):410–21.
3. Cheung Kevin J, Padmanaban Veena, Silvestri Vanesa, Schipper Koen, Cohen Joshua D, Fairchild Amanda N, Gorin Michael A, Verdone James E, Pienta Kenneth J, Bader Joel S, Ewald Andrew J. Polyclonal breast cancer metastases arise from collective dissemination of keratin 14-expressing tumor cell clusters. Proc Natl Acad Sci. 2016 Feb 16;113(7):E854–63.
4. Aceto Nicola, Bardia Aditya, Miyamoto David T, Donaldson Maria C, Wittner Ben S, Spencer Joel A, Yu Min, Pely Adam, Engstrom Amanda, Zhu Huili, Brannigan Brian W, Kapur Ravi, Stott Shannon L, Shioda Toshi, Ramaswamy Sridhar, Ting David T, Lin Charles P, Toner Mehmet, Haber Daniel A, et al. Circulating Tumor Cell Clusters Are Oligoclonal Precursors of Breast Cancer Metastasis. Cell. 2014 Aug;158(5):1110–22.
5. Tabassum Doris P, Polyak Kornelia. Tumorigenesis: it takes a village. Nat Rev Cancer. 2015 Aug 2;15(8):473–83.
6. Yeung Kay T, Yang Jing. Epithelial-mesenchymal transition in tumor metastasis. Mol Oncol. 2017 Jan;11(1):28–39.
7. Pignatelli Jeanine, Tumbarello David A, Schmidt Ronald P, Turner Christopher E. Hic-5 promotes invadopodia formation and invasion during TGF-β-induced epithelial-mesenchymal transition. J Cell Biol. 2012;197(3):421–37.
8. Eckert Mark A, Lwin Thinzar M, Chang Andrew T, Kim Jihoon, Danis Etienne, Ohno-Machado Lucila, Yang Jing. Twist1-Induced Invadopodia Formation Promotes Tumor Metastasis. Cancer Cell. 2011;19(3):372–86.
9. Eckert Mark A, Santiago-Medina Miguel, Lwin Thinzar M, Kim Jihoon, Courtneidge Sara A, Yang Jing. ADAM12 induction by Twist1 promotes tumor invasion and metastasis via regulation of invadopodia and focal adhesions. J Cell Sci. 2017 Jun 15;130(12):2036–48.
10. Karamanou Konstantina, Franchi Marco, Vynios Demitrios, Brézillon Stéphane. Epithelial-to-mesenchymal transition and invadopodia markers in breast cancer: Lumican a key regulator. Semin Cancer Biol. 2020 May;62(July 2019):125–33.
11. Murphy Danielle A, Courtneidge Sara A. The “ins” and “outs” of podosomes and invadopodia: characteristics, formation and function. Nat Rev Mol Cell Biol. 2011;12(7):413–26.
12. Eddy Robert J, Weidmann Maxwell D, Sharma Ved P, Condeelis John S. Tumor Cell Invadopodia: Invasive Protrusions that Orchestrate Metastasis. Trends Cell Biol. 2017 Aug;27(8):595–607.
13. Gligorijevic Bojana, Bergman Aviv, Condeelis John. Multiparametric classification links tumor microenvironments with tumor cell phenotype. PLoS Biol. 2014;12(11):e1001995.
14. Gligorijevic B, Wyckoff J, Yamaguchi H, Wang Y, Roussos ET, Condeelis J. N-WASP-mediated invadopodium formation is involved in intravasation and lung metastasis of mammary tumors. J Cell Sci. 2012;125(3):724–34.
15. Ye Xin, Weinberg Robert A. Epithelial-Mesenchymal Plasticity: A Central Regulator of Cancer Progression. Trends Cell Biol. 2015;25(11):675–86.
16. Cheung Kevin J, Gabrielson Edward, Werb Zena, Ewald Andrew J. Collective invasion in breast cancer requires a conserved basal epithelial program. Cell. 2013;155(7):1639–51.
17. Zhang Jian, Goliwas Kayla F, Wang Wenjun, Taufalele Paul V., Bordeleau Francois, Reinhart-King Cynthia A. Energetic regulation of coordinated leader–follower dynamics during collective invasion of breast cancer cells. Proc Natl Acad Sci. 2019 Apr

16;116(16):7867–72.
18. Wolf Katarina, Wu Yi I, Liu Yueying, Geiger Jörg, Tam Eric, Overall Christopher, Stack M Sharon, Friedl Peter. Multi-step pericellular proteolysis controls the transition from individual to collective cancer cell invasion. Nat Cell Biol. 2007;9(8):893–904.
19. Carey Shawn P, Starchenko Alina, McGregor Alexandra L, Reinhart-King Cynthia A. Leading malignant cells initiate collective epithelial cell invasion in a three-dimensional heterotypic tumor spheroid model. Clin Exp Metastasis. 2013;30(5):615–30.
20. Westcott Jill M, Prechtl Amanda M, Maine Erin A, Dang Tuyen T, Esparza Matthew A, Sun Han, Zhou Yunyun, Xie Yang, Pearson Gray W. An epigenetically distinct breast cancer cell subpopulation promotes collective invasion. J Clin Invest. 2015 May 1;125(5):1927–43.
21. Chapman Anna, Fernandez del Ama Laura, Ferguson Jennifer, Kamarashev Jivko, Wellbrock Claudia, Hurlstone Adam. Heterogeneous Tumor Subpopulations Cooperate to Drive Invasion. Cell Rep. 2014 Aug;8(3):688–95.
22. Bayarmagnai Battuya, Perrin Louisiane, Esmaeili Pourfarhangi Kamyar, Graña Xavier, Tüzel Erkan, Gligorijevic Bojana. Invadopodia-mediated ECM degradation is enhanced in the G1 phase of the cell cycle. J Cell Sci. 2019 Oct 15;132(20):jcs227116.
23. Miller BE, Miller FR, Wilburn DJ, Heppner GH. Analysis of tumour cell composition in tumours composed of paired mixtures of mammary tumour cell lines. Br J Cancer. 1987;56(5):561–9.
24. Dexter Daniel L, Kowalski Henryk M, Blazar BA, Fligiel Z, Vogel Renã, Heppner GH. Heterogeneity of tumor cells from a single mouse mammary tumor. Cancer Res. 1978 Oct;38(10):3174–81.
25. Aslakson CJ, Miller FR. Selective events in the metastatic process defined by analysis of the sequential dissemination of subpopulations of a mouse mammary tumor. Cancer Res. 1992 Mar 15;52(6):1399–405.
26. Seki Yoshinobu, Toba Ken, Fuse Ichiro, Sato Naoaki, Niwano Hiroe, Takahashi Hoyu, Tanabe Naohito, Aizawa Yoshifusa. In vitro effect of cyclosporin A, mitomycin C and prednisolone on cell kinetics in cultured human umbilical vein endothelial cells. Thromb Res. 2005 Jan;115(3):219–28.
27. Truong Hoa H, Xiong Jiangling, Ghotra Veerander PS, Nirmala Ella, Haazen Lizette, Le Devedec SE, Balcio lu HE, He Shuning, Snaar-Jagalska B Ewa, Vreugdenhil Erno, Meerman John HN, van de Water B, Danen Erik HJ. 1 Integrin Inhibition Elicits a Prometastatic Switch Through the TGF -miR-200-ZEB Network in E-Cadherin-Positive Triple-Negative Breast Cancer. Sci Signal. 2014 Feb 11;7(312):ra15–ra15.
28. Ilina Olga, Campanello Leonard, Gritsenko Pavlo G, Vullings Manon, Wang Chenlu, Bult Peter, Losert Wolfgang, Friedl Peter. Intravital microscopy of collective invasion plasticity in breast cancer. Dis Model Mech. 2018 Sep 1;11(9):dmm034330.
29. Lou Yuanmei, Preobrazhenska Olena, Auf Dem Keller Ulrich, Sutcliffe Margaret, Barclay Lorena, McDonald Paul C, Roskelley Calvin, Overall Christopher M, Dedhar Shoukat. Epithelial-Mesenchymal Transition (EMT) is not sufficient for spontaneous murine breast cancer metastasis. Dev Dyn. 2008;237(10):2755–68.
30. Sharma Ved P, Entenberg David, Condeelis John. High-Resolution Live-Cell Imaging and Time-Lapse Microscopy of Invadopodium Dynamics and Tracking Analysis. In: Coutts AS, editor. Methods in molecular biology (Clifton, NJ). Totowa, NJ: Humana Press; 2013. p. 343–57. (Methods in Molecular Biology; vol. 1046).
31. Pourfarhangi Kamyar Esmaeili, Bergman Aviv, Gligorijevic Bojana. ECM Cross-Linking Regulates Invadopodia Dynamics. Biophys J. 2018 Mar;114(6):1455–66.
32. Steinberg MS. Reconstruction of Tissues by Dissociated Cells. Science (80-). 1963 Aug 2;141(3579):401–8.
33. Smyrek I, Mathew B, Fischer SC, Lissek SM, Becker S, Stelzer EHK. E-cadherin, actin,

microtubules and FAK dominate different spheroid formation phases and important elements of tissue integrity. Biol Open. 2019 Jan 15;8(1):bio037051.

34. Cerchiari Alec E, Garbe James C, Jee Noel Y, Todhunter Michael E, Broaders Kyle E, Peehl Donna M, Desai Tejal A, LaBarge Mark A, Thomsonf Matthew, Gartner Zev J. A strategy for tissue self-organization that is robust to cellular heterogeneity and plasticity. Proc Natl Acad Sci U S A. 2015;112(7):2287–92.

35. Labernadie Anna, Kato Takuya, Brugués Agustí, Serra-Picamal Xavier, Derzsi Stefanie, Arwert Esther, Weston Anne, González-Tarragó Victor, Elosegui-Artola Alberto, Albertazzi Lorenzo, Alcaraz Jordi, Roca-Cusachs Pere, Sahai Erik, Trepat Xavier. A mechanically active heterotypic E-cadherin/N-cadherin adhesion enables fibroblasts to drive cancer cell invasion. Nat Cell Biol. 2017;19(3):224–37.

36. Yang Jing, Mani Sendurai a, Donaher Joana Liu, Ramaswamy Sridhar, Itzykson Raphael a, Come Christophe, Savagner Pierre, Gitelman Inna, Richardson Andrea, Weinberg Robert a. Twist, a Master Regulator of Morphogenesis, Plays an Essential Role in Tumor Metastasis. Cell. 2004 Jun;117(7):927–39.

37. Aiello Nicole M, Maddipati Ravikanth, Norgard Robert J, Balli David, Li Jinyang, Yuan Salina, Yamazoe Taiji, Black Taylor, Sahmoud Amine, Furth Emma E, Bar-Sagi Dafna, Stanger Ben Z. EMT Subtype Influences Epithelial Plasticity and Mode of Cell Migration. Dev Cell. 2018;45(6):681-695.e4.

38. Nieto M Angela, Huang Ruby Yun YJ, Jackson Rebecca AA, Thiery Jean Paul P. Emt: 2016. Cell. 2016;166(1):21–45.

39. Padmanaban Veena, Krol Ilona, Suhail Yasir, Szczerba Barbara M, Aceto Nicola, Bader Joel S, Ewald Andrew J. E-cadherin is required for metastasis in multiple models of breast cancer. Nature. 2019 Sep 4;573(7774):439–44.

40. Tester Angus M, Ruangpanit Neeracha, Anderson Robin L, Thompson Erik W. MMP-9 secretion and MMP-2 activation distinguish invasive and metastatic sublines of a mouse mammary carcinoma system showing epithelial-mesenchymal transition traits. Clin Exp Metastasis. 2000;18(7):553–60.

41. Johnstone Cameron N, Smith Yvonne E, Cao Yuan, Burrows Allan D, Cross RSN, Ling Xiawei, Redvers Richard P, Doherty Judy P, Eckhardt Bedrich L, Natoli Anthony L, Restall Christina M, Lucas Erin, Pearson Helen B, Deb Siddhartha, Britt Kara L, Rizzitelli Alexandra, Li Jason, Harmey Judith H, Pouliot Normand, et al. Functional and molecular characterisation of EO771.LMB tumours, a new C57BL/6-mouse-derived model of spontaneously metastatic mammary cancer. Dis Model Mech. 2015 Mar 1;8(3):237–51.

42. Heisenberg Carl-Philipp, Bellaïche Yohanns. Forces in Tissue Morphogenesis and Patterning. Cell. 2013 May;153(5):948–62.

43. Beatrici Carine P, Brunnet Leonardo G. Cell sorting based on motility differences. Phys Rev E. 2011 Sep 27;84(3):031927.

44. Mori Hidetoshi, Gjorevski N, Inman Jamie L, Bissell Mina J, Nelson Celeste M. Self-organization of engineered epithelial tubules by differential cellular motility. Proc Natl Acad Sci. 2009 Sep 1;106(35):14890–5.

45. Pawlizak Steve, Fritsch Anatol W, Grosser Steffen, Ahrens Dave, Thalheim Tobias, Riedel Stefanie, Kießling Tobias R, Oswald Linda, Zink Mareike, Manning M Lisa, Käs Josef A. Testing the differential adhesion hypothesis across the epithelial−mesenchymal transition. New J Phys. 2015 Aug 25;17(8):083049.

46. Villeneuve Clémentine, Lagoutte Emilie, de Plater Ludmilla, Mathieu Samuel, Manneville Jean-Baptiste, Maître Jean-Léon, Chavrier Philippe, Rossé Carine. aPKCi triggers basal extrusion of luminal mammary epithelial cells by tuning contractility and vinculin localization at cell junctions. Proc Natl Acad Sci. 2019 Nov 26;116(48):24108–14.

47. Perrin Louisiane, Tucker Theodore, Gligorijevic Bojana. Time-Resolved Fluorescence

Imaging and Analysis of Cancer Cell Invasion in the 3D Spheroid Model. J Vis Exp. 2021 Jan 30;(167):1–14.

48. Chen Wen-Tien, Yeh Yunyun, Nakahara Hirokazu. An in vitro cell invasion assay: Determination of cell surface proteolytic activity that degrades extracellular matrix. J Tissue Cult Methods. 1994 Sep;16(3–4):177–81.
49. Tinevez Jean-Yves, Perry Nick, Schindelin Johannes, Hoopes Genevieve M, Reynolds Gregory D, Laplantine Emmanuel, Bednarek Sebastian Y, Shorte Spencer L, Eliceiri Kevin W. TrackMate: An open and extensible platform for single-particle tracking. Methods. 2017 Feb;115:80–90.
50. Di Martino Julie, Henriet Elodie, Ezzoukhry Zakaria, Mondal Chandrani, Bravo-Cordero Jose Javier, Moreau Violaine, Saltel Frederic. 2D and 3D Matrices to Study Linear Invadosome Formation and Activity. J Vis Exp. 2017;(124):1–9.
51. Konen J, Summerbell E, Dwivedi B, Galior K, Hou Y, Rusnak L, Chen A, Saltz J, Zhou W, Boise LH, Vertino P, Cooper L, Salaita K, Kowalski J, Marcus AI. Image-guided genomics of phenotypically heterogeneous populations reveals vascular signalling during symbiotic collective cancer invasion. Nat Commun. 2017 Aug 12;8(1):15078.
52. Tasoglu Savas, Safaee Hooman, Zhang Xiaohui, Kingsley James L., Catalano Paolo N., Gurkan Umut Atakan, Nureddin Aida, Kayaalp Emre, Anchan Raymond M., Maas Richard L., Tüzel Erkan, Demirci Utkan. Exhaustion of Racing Sperm in Nature-Mimicking Microfluidic Channels During Sorting**. Small 2013** October 25; 9(20):doi:10.1002/smll.201300020.
53. Pulaski Beth A, Ostrand-Rosenberg Suzanne. Mouse 4T1 Breast Tumor Model. Curr Protoc Immunol. 2000;39(1):1–16.

Acknowledgments

We would like to thank members of Temple Bioengineering and Fox Chase Cancer Center Biology for valuable discussions. We thank David Ambrose at the flow cytometry core (Lewis Katz School of Medicine) for his assistance with cell sorting. We also thank our funding resources: American Cancer Society Research Scholar Grant 134415-RSG-20-034-01-CSM, Conquer Cancer Now/Young Investigator Award, National Institutes of Health, R00 CA172360 and R01 CA230777, all to BG.

The authors have no competing financial interests.

Conceptualization: L.P., B.G.; Methodology: L.P., B.G.; Investigation: L.P., B.B., B.G.; Formal analysis: L.P., E.T.; Resources: B.G.; Writing - original draft: L.P.; Writing - review & editing: L.P., B.G.; Visualization: L.P.; Supervision: B.G.; Project administration: B.G.; Funding acquisition: B.G.

Figures

Fig. 1. 4T1 cells, but not 67NR cells, exhibit MMP-dependent spheroid invasion.
(**A**) Representative micrographs (maximum projection) of 4T1 and 67NR spheroids grown in a 3D collagen I matrix for 2 days. Nuclei were stained with DAPI. Spheroids were treated from day 0 with a pan-MMP inhibitor (GM6001, top right panel), a mitosis inhibitor (mitomycin C, Mito C, bottom right panel) or DMSO control. Scale bars: 100 µm. (**B**) Quantification of the spheroid area as a function of time for 4T1 and 67NR cells from (**A**). *P*=0.0006, 0.0001, 0.1254 and 0.0571 were obtained by the two sample t-test. (**C**) Representative micrographs of a 4T1 strand 2 days after the spheroid was embedded in a 3D collagen I matrix. The spheroid was immunolabeled for MMP-mediated cleaved collagen I (Col-3/4, green). F-actin (phalloidin, magenta) and nuclei (DAPI, blue) were stained. Scale bar: 50 µm. (**D**) Western blot analysis of Tks5 and cortactin expression levels in 4T1 and 67NR cells. β-actin is used as a loading control. (**E**) Representative micrographs of gelatin degradation for 4T1 (top panel) and 67NR (bottom panel) cells 18 h post plating. The inserts show a 4X zoom-in of the boxed area and arrowheads indicate representative degradation holes. Scale bars: 20 µm. (**F**) Quantification of the degradation area per cell for 4T1 and 67NR cells from (**E**). *P*<4.40e-16 was obtained by the Wilcoxon rank sum test. (**G**) Representative micrographs of 4T1 cells grown on fluorescent gelatin (gray), immunolabeled for Tsk5 (green) and with labeled F-actin (phalloidin, magenta). The inserts show a 2X zoom-in of the boxed area and arrowheads indicate representative mature invadopodia. Scale bar: 10 µm. (**H**) Representative micrographs of a 4T1 strand 2 days after the spheroid was embedded in a 3D collagen I matrix. The spheroid was immunolabeled for Tks5 (green) and MMP-mediated cleaved collagen I (C-3/4, cyan). F-actin (phalloidin, magenta) was stained. The inserts show a 1.25X zoom-in of the boxed area. Scale bar: 30 µm. (**I**) Representative snapshot micrographs of a 4T1 (left panel) and a 67NR (right panel) monolayer 24 h post wounding. Representative cell trajectories are shown. Scale bars: 100 µm. (**J**) Trajectories of 4T1 (top panel) and 67NR (bottom panel) cells from the wound assay. The wound was cross-shaped. (**K**) Quantification of the instantaneous speed of 4T1 and 67NR cells from (**J**). *P*=1.167e-13 was obtained by the Wilcoxon rank sum test. (**L**) Quantification of the persistence of 4T1 and 67NR cells from (**J**). *P*<2.2e-16 was obtained by the Wilcoxon rank sum test. All data are represented as boxplots with median (line), 25th/75th percentiles (boxes) and maximum/minimum (whiskers). Statistical significance was defined as *p<0.05, **p<0.01 and ***p<0.001. Additional information on the metrics and statistics can be found in the Table S1.

Fig. 2. Prior to invasion, 4T1 cells sort from 67NR cells.
(**A**) Representative micrographs (maximum projection) of a mixed spheroid, with a 1 to 50 ratio of 4T1-mScarlet (magenta) to 67NR-GFP (green) cells, grown in a 3D collagen I matrix and imaged daily. Day 1 indicate day 1 post embedding. Scale bars: 100 µm. (**B**) Coordinates of 4T1-mScarlet (4T1-mScar, magenta crosses) and 67NR-GFP (green crosses) cells from all mixed spheroids presented in (**A**) and fig. S3C. (**C**) Schematic representation of the distance index. (**D**) Quantification of the distance index (DI) for 4T1-mScarlet (4T1-mScar, magenta boxes) and 67NR-GFP (green boxes) cells from (**A, B**). *P*=0.7747, 0.0983, 1.32e-14 and <2.2e-16 were obtained by the Wilcoxon rank sum test. (**E**) Representative micrographs (median slice) of mixed spheroids grown in a 3D collagen I matrix for 3 or 4 days. Spheroids were treated from day 0 with an inhibitor of cell contractility (ROCK inhibitor, Y-27632, top panels) or a pan-MMP inhibitor (GM6001, bottom panels). Scale bar: 100 µm. (**F**) Quantification of the distance index (DI) for 4T1-mScarlet (4T1-mScar, magenta boxes) and 67NR-GFP (green boxes) cells from (**E**). *P*=0.5694, 0.9285, 0.2821 and 0.428 were obtained by the Wilcoxon rank sum test. (**G**) Schematic representation of the edge (dark gray) and core (light gray) compartments in a spheroid. (**H**) Representative snapshot micrographs (single slice) of a mixed spheroid grown in a 3D collagen I matrix. The time-lapse started 10 h post embedding and lasted for 44 h. For 4T1-mScarlet and 67NR-GFP cells,

representative cell trajectories in the edge and core compartments are shown (right panels). The trajectories are color-coded according to time. Scale bars: 100 µm. (**I**) Quantification of the Δ distance index (ΔDI) for 4T1-mScarlet (4T1-mScar, magenta boxes) and 67NR-GFP (green boxes) cells from (**H**). Spheroids were treated from day 0 with DMSO control (left panel) or a pan-MMP inhibitor (GM6001, right panel). *P*=0.0204, 0.7466, 0.8438 and 0.1064 were obtained by the Wilcoxon rank sum test. All data are represented as boxplots with median (line), 25th/75th percentiles (boxes) and maximum/minimum (whiskers). Statistical significance was defined as *p<0.05, **p<0.01, ***p<0.001. Additional information on the metrics and statistics can be found in the Table S1.(**J**) Radial MSDs and PRW fits for the 4T1-mScarlet in the edge (black circles, purple line, top) and core compartments (black squares, purple line, bottom) and 67NR-GFP cells in the edge (red circles, green line, top) and core compartments (red squares, green line, bottom). Only DMSO control spheroids are shown for clarity. (**K**) Cell speeds and (**L**) Persistence lengths calculated from the PRW fits.

Fig. 3. 4T1, but not 67NR, cells are sensitive to the presence of adhesive ECM.
(**A**) Representative micrographs (median slice) of mixed spheroids grown in an agarose matrix for 3 or 4 days. Scale bar: 100 µm. (**B**) Quantification of the distance index (DI) for 4T1-mScarlet (4T1-mScar, magenta boxes) and 67NR-GFP (green boxes) cells from (**A**). *P*=0.3221 and 0.99 were obtained by the Wilcoxon rank sum test. (**C**) Representative snapshot micrographs (single slice) of a mixed spheroid grown in a 3D collagen I matrix. 4T1-mScarlet cells are shown. The time-lapse started 10 h post embedding and lasted for 44 h. Representative cell trajectories in the edge and core compartments are shown (right panels). The trajectories are color-coded according to time. Scale bar: 100 µm. (**D**) Quantification of the Δ distance index (ΔDI) for 4T1-mScarlet cells from (**C**). *P*=0.0008 was obtained by the Wilcoxon rank sum test. (**E**) Schematic representation of the 2D cell-ECM competition assay and representative micrographs of cells present at the gelatin/poly-L-lysine (PLL) interface 24 h post plating (top, right panel). 4T1-mScarlet (4T1-mScar; bottom, left panel) and 67NR-GFP (bottom, right panel) cells were plated on the gelatin islands only. Scale bar: 200 µm. (**F**) Quantification of the % of 4T1-mScarlet (4T1-mScar, magenta boxes) and 67NR-GFP (green boxes) cells on poly-L-lysine (PLL) from (**E**). (**G**) Schematic representation of the contact angle (θ) and representative micrographs (orthogonal views) of 4T1-mScarlet and 67NR-GFP cells on poly-L-lysine (PLL) or gelatin, 5 h post plating. Scale bar: 5 µm. (**H**) Quantification of the contact angle θ for cells from (**G**). PLL, 4T1 *vs.* 67NR: *P*=1.25e-09; gelatin, 4T1 *vs.* 67NR: *P*=0.5626; 4T1, PLL *vs.* gelatin: *P*=4.13e-10 and 67NR, PLL *vs.* gelatin: *P*=0.05706 were obtained by the Wilcoxon rank sum test. All data are represented as boxplots with median (line), 25th/75th percentiles (boxes) and maximum/minimum (whiskers). Statistical significance was defined as *p<0.05, **p<0.01, ***p<0.001. Additional information on the metrics and statistics can be found in the Table S1.

Fig. 4. 4T1 cells lead 67NR cells in an MMP-dependent cooperative invasion.
(**A**) Representative micrographs (maximum projection) of spheroids made of a single or mixed 4T1-mScarlet and 67NR-GFP cell line, grown in a 3D collagen I matrix for 6 days. Mixed spheroids were made at a 1 to 50 ratio of 4T1-mScarlet to 67NR-GFP cells. Single spheroids were made in accordance with this ratio. Spheroids were treated from day 0 with a pan-MMP inhibitor (GM6001, right panel) or DMSO control. Scale bars: 100 µm. (**B-D**) Quantification of the number of strands per spheroid (**B**), the number of 67NR+ strands per spheroid (**C**) and the % of strands led by 4T1-mScarlet (4T1-mScar, magenta box) or 67NR-GFP (green boxes) cells (**D**) for single or mixed (white box) spheroids from (**A**). The red empty signs indicate zeros. *P*=1.9e-07 (**B**) and 9.86e-06 (**C**) were obtained by the Wilcoxon rank sum test. (**E**) Representative micrographs (median slice) of mixed spheroids from (**A**). Scale bars: 100 µm. (**F**) Coordinates of 4T1-mScarlet (4T1-mScar, magenta crosses) and 67NR-GFP (green crosses) cells from mixed spheroids in (**A**) and (**E**). (**G**)

Quantification of the distance index (DI) for 4T1-mScarlet (magenta boxes) and 67NR-GFP (green boxes) cells from (**E, F**). *P*<2.2e-16, 0.066 and <2.2e-16 were obtained by the Wilcoxon rank sum test. All data are represented as boxplots with median (line), 25th/75th percentiles (boxes) and maximum/minimum (whiskers). Statistical significance was defined as *p<0.05, **p<0.01 and ***p<0.001. Additional information on the metrics and statistics can be found in the Table S1.

Fig. 5. Cells with and without invadopodia cooperate for invasion and lung metastasis. (**A**) Western blot analysis of E/N-cadherin, Tks5 and cortactin expression levels in 4T1-shControl (4T1-CTL) and 4T1-mScarlet-mTks5 KD (4T1-KD) cells. β-actin is used as a loading control. (**B**) Representative micrographs of gelatin degradation for 4T1-shControl (4T1-CTL, top panels) and 4T1-mScarlet-mTks5 KD (4T1-KD, bottom panels) cells 18 h after plating. The inserts show a 2X zoom-in of the boxed area and arrowheads indicate representative degradation holes. Scale bar: 20 µm. (**C**) Quantification of the degradation area per cell for 4T1-shControl (4T1-CTL) and 4T1-mScarlet-mTks5 KD (4T1-KD) cells from (**B**). *P*=7.24e-14 was obtained by the Wilcoxon rank sum test. (**D**) Representative micrographs (maximum projection) of spheroids made of a single or mixed 4T1-shControl (4T1-CTL) and 4T1-mScarlet-mTks5 KD (4T1-KD) cell line, grown in a 3D collagen I matrix for 2 days. Mixed spheroids were made at a 1 to 1 ratio. Scale bar: 100 µm. (**E-G**) Quantification of the number of strands per spheroid (**E**), the number of KD+ strands per spheroid (**F**) and the % of strands led by 4T1-shControl (4T1-CTL) or 4T1-mScarlet-mTks5 KD (4T1-KD) cells (**G**) for single or mixed spheroids from (**D**). *P*<2.2e-16 was obtained by the two-sample t-test, *P*=7.26e-07 and 0.3802 were obtained by the Welch two-sample t-test in (**E**). *P*=8.488e-07 was obtained by the Welch two-sample t-test in (**F**). (**H**) Representative micrographs (maximum projection) of a mixed 4T1-mScarlet-mTks5 KD (4T1-KD) and 67NR-GFP spheroid, grown in a 3D collagen I matrix for 6 days. Mixed spheroids were made at a 1 to 50 ratio. Scale bar: 100 µm. (**I**) Quantification of the number of strands per spheroid for mixed spheroids from Fig. 4A (4T1+67NR) and (**H**) (4T1-KD+67NR). *P*=3.36e-06 was obtained by the Wilcoxon rank sum test. (**J**) Quantification of the number of colonies per cm^2 from the lung clonogenic assay. Mice were inoculated with a single (plus symbols) or mixed (crosses) 4T1-shControl (4T1-CTL, black) and 4T1-mScarlet-mTks5 KD (4T1-KD, magenta) cell lines. Except in (**J**), all data are represented as boxplots with median (line), 25th/75th percentiles (boxes) and maximum/minimum (whiskers). Statistical significance was defined as *p<0.05, **p<0.01 and ***p<0.001. Additional information on the metrics and statistics can be found in the Table S1.

Fig. 1

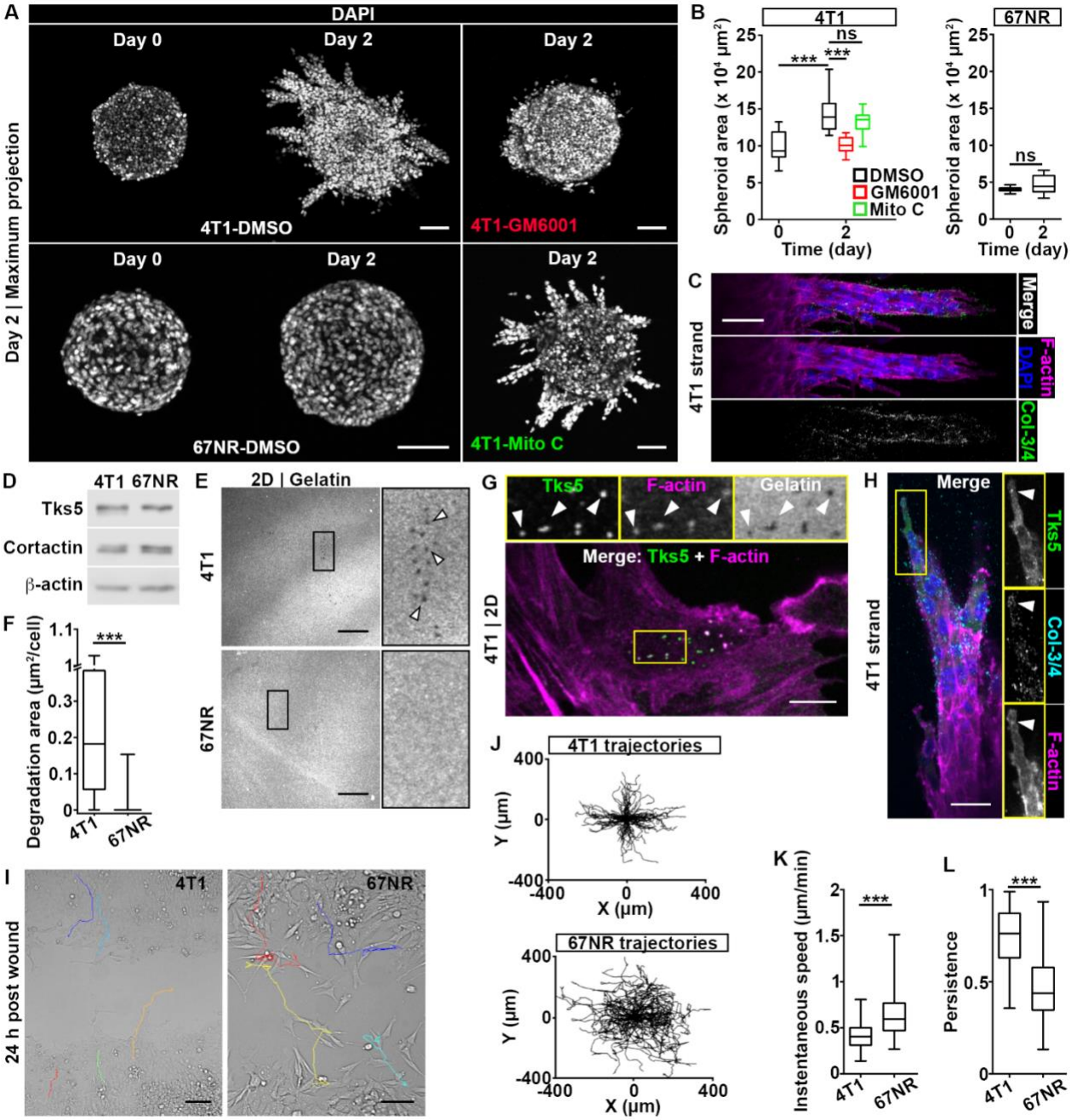
A
DAPI
Day 0
Day 2
Day 2
4T1-DMSO
4T1-GM6001
Day 0
Day 2
Day 2
67NR-DMSO
4T1-Mito C
Day 2 | Maximum projection
B
4T1
67NR
Spheroid area (x 10⁴ µm²)
Time (day)
***
***
ns
ns
DMSO
GM6001
Mito C
C
4T1 strand
Merge
F-actin
DAPI
Col-3/4
D
4T1 67NR
Tks5
Cortactin
β-actin
E
2D | Gelatin
4T1
67NR
F
Degradation area (µm²/cell)
***
4T1
67NR
G
Tks5
F-actin
Gelatin
Merge: Tks5 + F-actin
4T1 | 2D
H
Merge
4T1 strand
Tks5
Col-3/4
F-actin
I
4T1
67NR
24 h post wound
J
4T1 trajectories
67NR trajectories
Y (µm)
X (µm)
K
Instentaneous speed (µm/min)
***
4T1
67NR
L
Persistence
***
4T1
67NR

Fig. 2

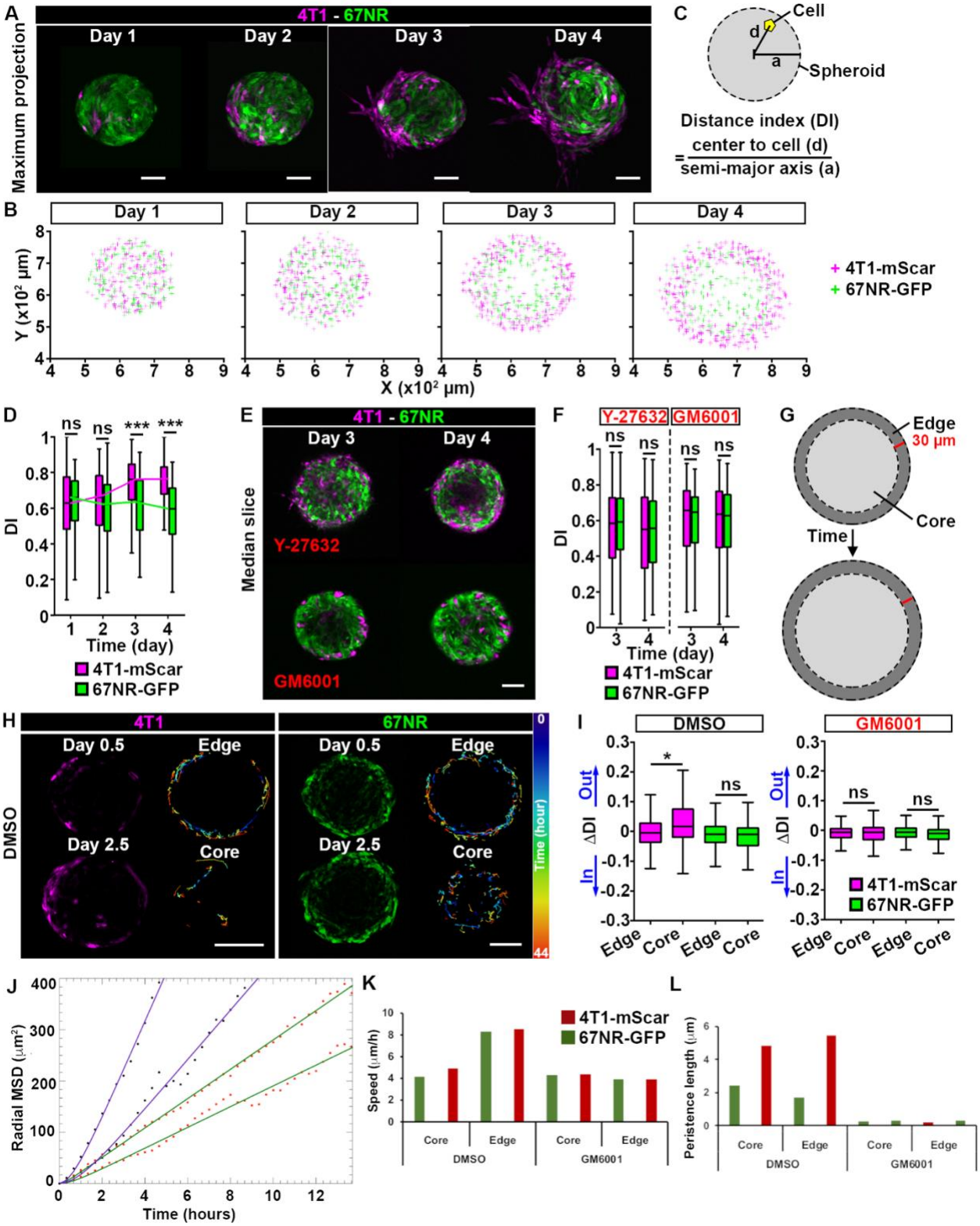
A
4T1 - 67NR
Day 1
Day 2
Day 3
Day 4
Maximum projection
C
Cell
d
a
Spheroid
Distance index (DI)
= center to cell (d) / semi-major axis (a)
B
Day 1
Day 2
Day 3
Day 4
Y (x10² µm)
X (x10² µm)
4T1-mScar
67NR-GFP
D
ns
ns
***
***
DI
Time (day)
4T1-mScar
67NR-GFP
E
4T1 - 67NR
Day 3
Day 4
Median slice
Y-27632
GM6001
F
Y-27632
GM6001
ns
DI
Time (day)
4T1-mScar
67NR-GFP
G
Edge
30 µm
Core
Time
H
4T1
67NR
DMSO
Day 0.5
Edge
Day 2.5
Core
Time (hour)
0
44
I
DMSO
GM6001
Out
In
ΔDI
*
ns
Edge
Core
4T1-mScar
67NR-GFP
J
Radial MSD (µm²)
Time (hours)
K
4T1-mScar
67NR-GFP
Speed (µm/h)
Core
Edge
DMSO
GM6001
L
Peristence length (µm)
Core
Edge
DMSO
GM6001

Fig. 3

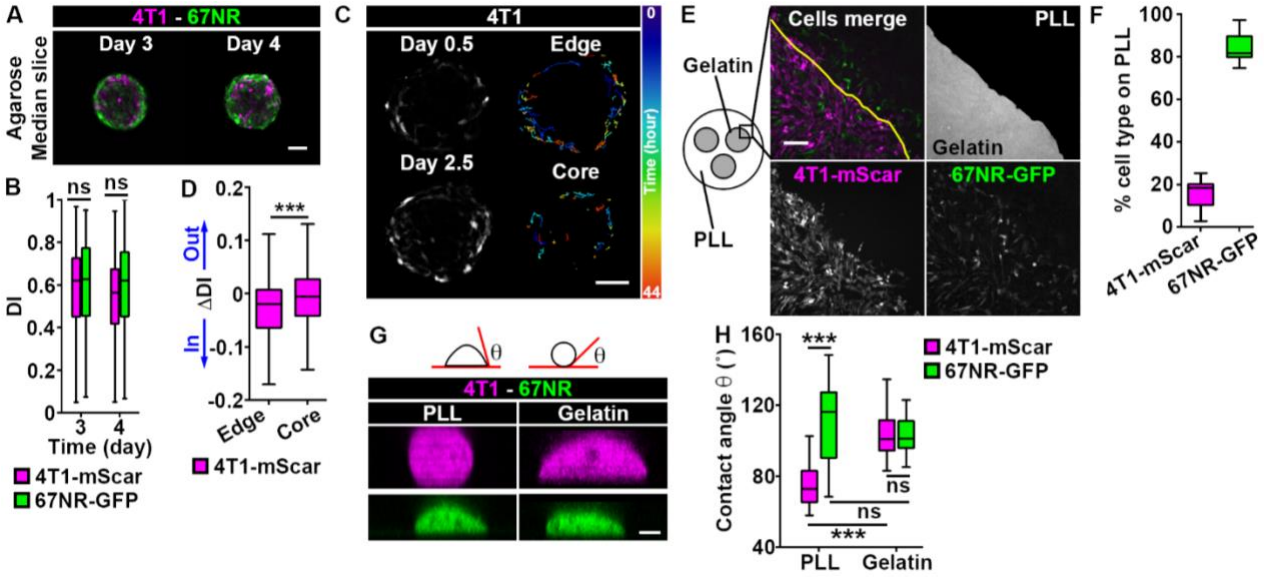
A
4T1 - 67NR
Day 3
Day 4
Agarose
Median slice
B
ns
ns
DI
Time (day)
4T1-mScar
67NR-GFP
D
***
Out
In
ΔDI
Edge
Core
4T1-mScar
C
4T1
Day 0.5
Edge
Day 2.5
Core
Time (hour)
E
Cells merge
PLL
Gelatin
4T1-mScar
67NR-GFP
F
% cell type on PLL
4T1-mScar
67NR-GFP
G
θ
4T1 - 67NR
PLL
Gelatin
H
Contact angle θ (°)
***
ns
ns
***
PLL
Gelatin
4T1-mScar
67NR-GFP

Fig. 4

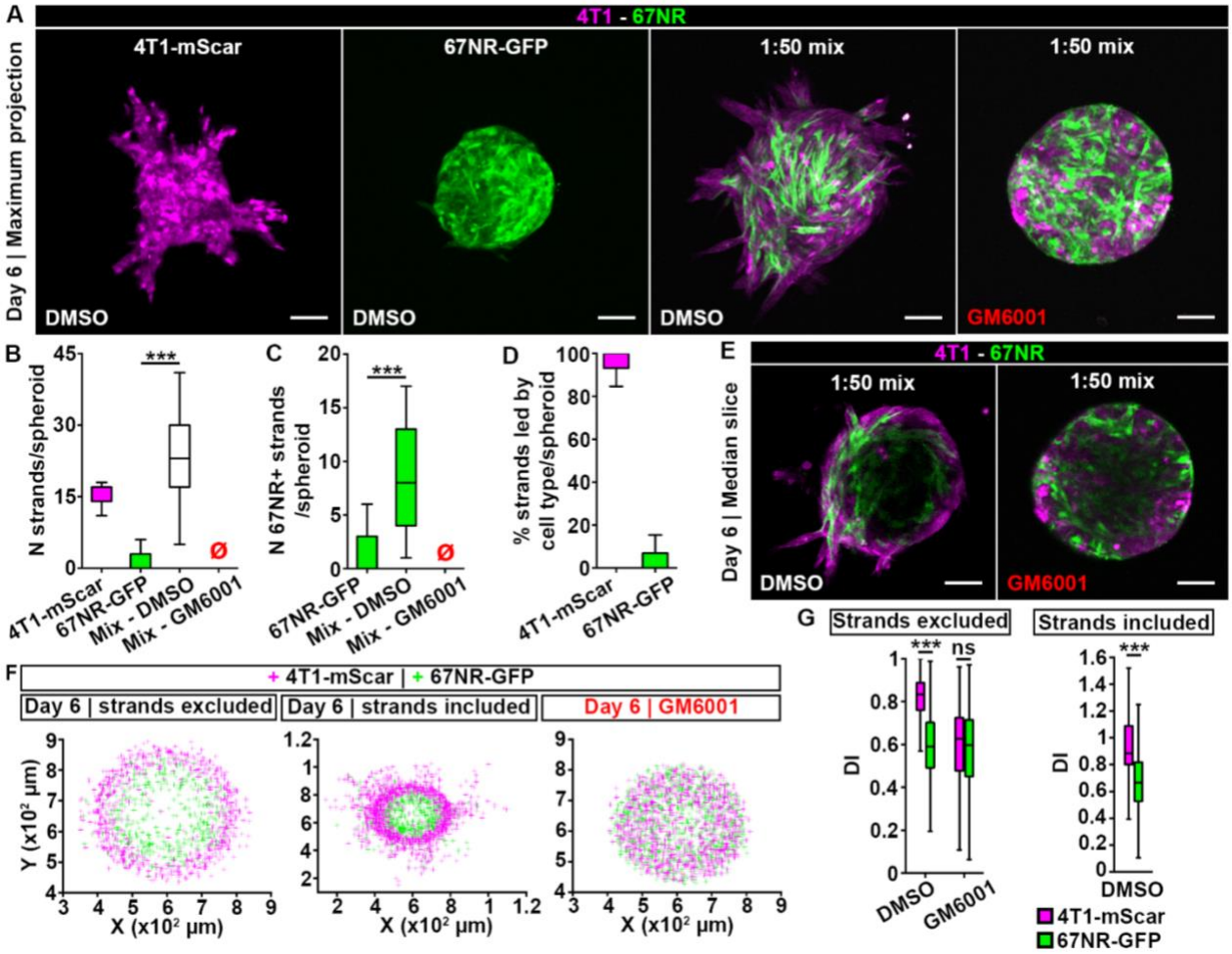
A
4T1 - 67NR
Day 6 | Maximum projection
4T1-mScar
67NR-GFP
1:50 mix
1:50 mix
DMSO
DMSO
DMSO
GM6001
B
N strands/spheroid
***
Ø
4T1-mScar
67NR-GFP
Mix - DMSO
Mix - GM6001
C
N 67NR+ strands /spheroid
***
Ø
67NR-GFP
Mix - DMSO
Mix - GM6001
D
% strands led by cell type/spheroid
4T1-mScar
67NR-GFP
E
4T1 - 67NR
Day 6 | Median slice
1:50 mix
1:50 mix
DMSO
GM6001
F
+ 4T1-mScar | + 67NR-GFP
Day 6 | strands excluded
Day 6 | strands included
Day 6 | GM6001
Y (x10² µm)
X (x10² µm)
X (x10² µm)
X (x10² µm)
G
Strands excluded
Strands included
***
ns
***
DI
DI
DMSO
GM6001
DMSO
4T1-mScar
67NR-GFP

Fig. 5

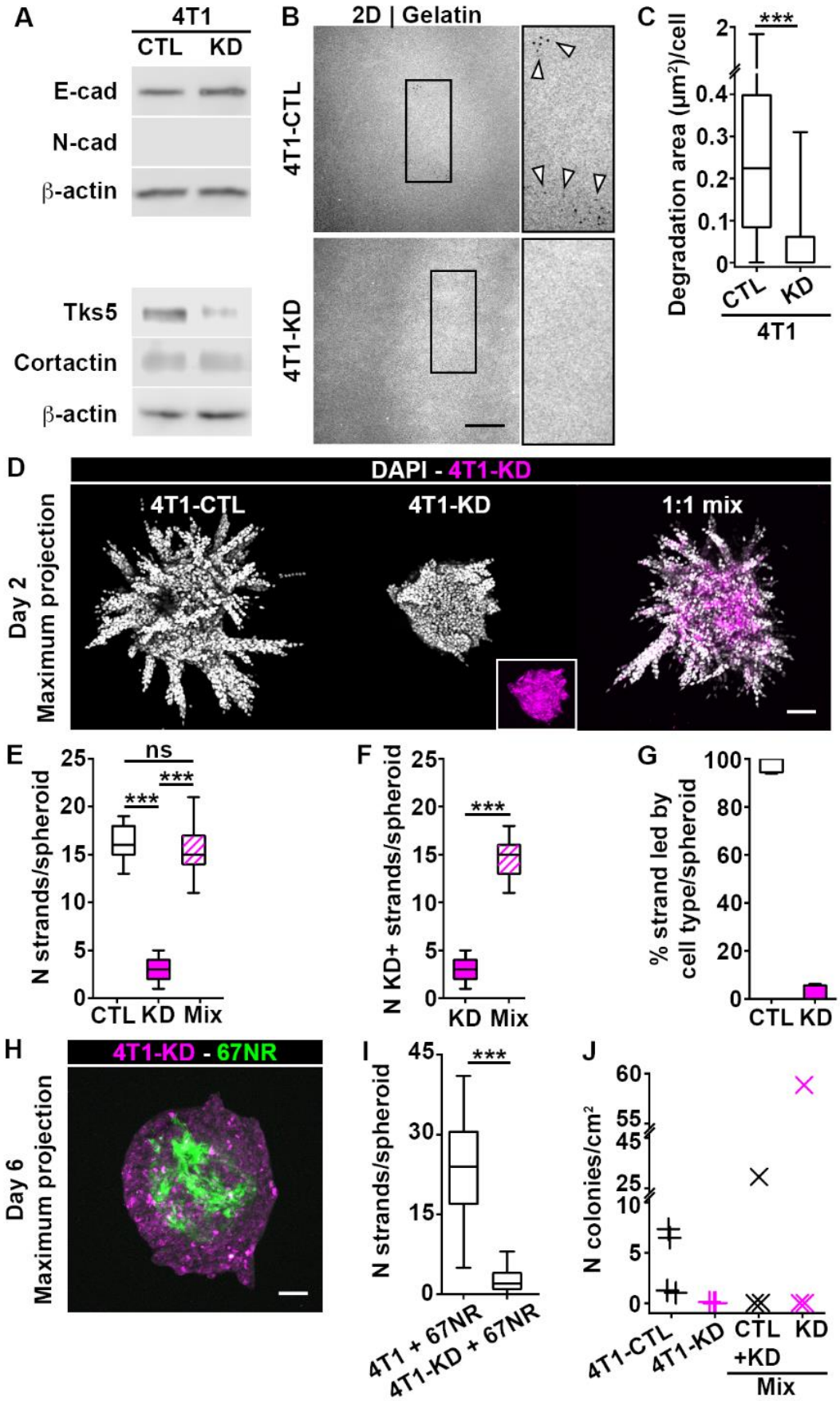
A
4T1
CTL
KD
E-cad
N-cad
β-actin
Tks5
Cortactin
β-actin
B
2D | Gelatin
4T1-CTL
4T1-KD
C
***
Degradation area (μm²)/cell
CTL
KD
4T1
D
DAPI - 4T1-KD
4T1-CTL
4T1-KD
1:1 mix
Day 2
Maximum projection
E
ns
***
***
N strands/spheroid
CTL KD Mix
F
***
N KD+ strands/spheroid
KD Mix
G
% strand led by cell type/spheroid
CTL KD
H
4T1-KD - 67NR
Day 6
Maximum projection
I
***
N strands/spheroid
4T1 + 67NR
4T1-KD + 67NR
J
N colonies/cm²
4T1-CTL
4T1-KD
CTL +KD
KD
Mix